

Electromagnetic calorimeters based on scintillating lead tungstate crystals for experiments at Jefferson Lab [☆]

A.Asaturyan^a, F.Barbosa^c, V.Berdnikov^b, E.Chudakov^c, J.Crafts^{b,c}, H.Egiyan^c,
L.Gan^f, A.Gasparian^g, K.Harding^c, T.Horn^b, V.Kakoyan^a, H.Mkrtchyan^a,
Z.Papandreou^e, V. Popov^c, N.Sandoval^c, A.Somov^{c,*}, S.Somov^d, A. Smith^h, C.
Stanislav^c, S.Taylor^c, H. Voskanyan^a, T. Whitlatch^c, S. Worthington^c

^aA. I. Alikhanian National Science Laboratory (Yerevan Physics Institute), 0036 Yerevan, Armenia

^bThe Catholic University of America, Washington, DC 20064, USA

^cThomas Jefferson National Accelerator Facility, Newport News, VA 23606, USA

^dNational Research Nuclear University MEPhI, Moscow 115409, Russia

^eUniversity of Regina, Regina, Saskatchewan, Canada S4S 0A2

^fUniversity of North Carolina at Wilmington, Wilmington, NC 28403, USA

^gNorth Carolina A&T State University, Greensboro, NC 27411, USA

^hDuke University, Durham, NC 27708, USA

Abstract

A new electromagnetic calorimeter consisting of 140 lead tungstate (PbWO₄) scintillating crystals was constructed for the PrimEx- η experiment at Jefferson lab. The calorimeter was integrated into the data acquisition and trigger systems of the GlueX detector and used in the experiment to reconstruct Compton scattering events. The experiment started collecting data in the spring of 2019 and acquired about 30% of the required statistics. The calorimeter is a prototype for two PbWO₄-based detectors: the Neutral Particle Spectrometer (NPS) and the lead tungstate insert of the Forward CALorimeter (FCAL) of the GlueX detector. The article presents the design and performance of the Compton calorimeter and gives a brief overview of the FCAL and NPS projects.

Keywords: Electromagnetic calorimeter, Lead tungstate scintillator

[☆]Notice: Authored by Jefferson Science Associates, LLC under U.S. DOE Contract No. DE-AC05-06OR23177. The U.S. Government retains a non-exclusive, paid-up, irrevocable, world-wide license to publish or reproduce this manuscript for U.S. Government purposes.

*Corresponding author. Tel.: +1 757 269 5553; fax: +1 757 269 6331.

Email address: somov@jlab.org (A.Somov)

1. Introduction

Electromagnetic calorimeters based on PbWO_4 scintillating crystals have a widespread application in experiments at different accelerator facilities such as CERN, FNAL, GSI, and Jefferson Lab (JLab) [1–5]. The small radiation length ($L_R = 0.89$ cm) and Molière radius ($R_M = 2.19$ cm) of PbWO_4 allows to build high-granularity radiation hard detectors with a good spatial separation and energy resolution of reconstructed electromagnetic showers, which makes these crystals the material of choice in many of these applications.

In this article we describe the design, construction, and performance of a calorimeter composed of 140 rectangular 2.05 cm \times 2.05 cm \times 20 cm PbWO_4 scintillating crystals, recently produced by Shanghai Institute of Ceramics (SICCAS). The calorimeter was used in the PrimEx- η experiment [6] with the GlueX detector [7] in the spring of 2019 to reconstruct Compton scattering events and is referred to as the Compton CALorimeter (CCAL).

The CCAL is a prototype for two large-scale PbWO_4 -based detectors which are currently under construction in experimental Hall D and Hall C at Jefferson Lab: (1) the lead tungstate insert of the Forward CALorimeter (FCAL) of the GlueX detector and (2) the electromagnetic calorimeter of the Neutral Particle Spectrometer (NPS) [8]. The new calorimeters will be based on the PbWO_4 crystals of the same size as in the CCAL and use the same type of photodetectors and readout electronics. The crystals will be procured from two vendors: SICCAS in China and CRYTUR in the Czech Republic. PbWO_4 crystals are also being considered for an electromagnetic calorimeter of the future Electron-Ion Collider (EIC) [9].

The lead tungstate insert of the FCAL consists of 1596 high-granularity, high resolution PbWO_4 crystals, which will be used to replace the lead glass modules in the inner part of the FCAL. This upgrade will improve the separation of showers and the shower energy resolution in the forward direction, which is required by the JLab Eta Factory (JEF) experiment to perform precision measurements of various $\eta^{(\prime)}$ decays

29 with emphasis on rare neutral modes [10]. The design of the FCAL PbWO₄ module ¹,
30 is based on that of the CCAL, except for some small modifications required to shield
31 the magnetic field present in the calorimeter region. Studies of the magnetic shield-
32 ing of photomultiplier tubes (PMT), and the design of the FCAL PbWO₄ module will
33 be described in this article. The detector rates and operating conditions expected for
34 the FCAL lead-tungstate insert were evaluated by using the CCAL during a few short
35 GlueX physics runs at high luminosity. The measurements provided important infor-
36 mation needed to optimize the design of the PMT divider and amplifier for GlueX run
37 conditions.

38 The Neutral Particle Spectrometer [8] in experimental Hall C will consist of a
39 PbWO₄ electromagnetic calorimeter preceded by a sweeping magnet. The NPS is re-
40 quired by Hall C's precision cross section measurement program with neutral final
41 states [11–16]. Such precision measurements of small cross sections play a central role
42 in studies of transverse spatial and momentum hadron structure. The NPS detector will
43 consist of 1080 PbWO₄ crystals arranged in a 30 × 36 array.

44 Experience gained during fabrication and operation of the CCAL was critical for
45 finalizing the design of the FCAL insert and also helped further optimize the NPS
46 calorimeter. This article is organized as follows: we will present the PrimEx- η ex-
47 periment and performance of the CCAL in Section 2 and Section 3, and will briefly
48 describe the FCAL and NPS projects in Sections 4 and 5.

49 **2. PrimEx- η experiment with the GlueX detector**

50 The GlueX detector [7] was designed to perform experiments using a photon beam.
51 Photons are produced via the bremsstrahlung process by electrons, provided by the
52 JLab electron accelerator facility, incident on a thin radiator. The energy of a beam
53 photon (E_γ) is determined by detecting a scattered electron after radiating the photon
54 as follows: $E_\gamma = E_e - E'_e$, where E_e is the primary electron beam energy and E'_e is the
55 energy of the bremsstrahlung electron. The bremsstrahlung electron is deflected in a 6

¹The module consists of a PbWO₄ crystal wrapped with the light reflective foil and coupled to the pho-
tomultiplier tube with the divider.

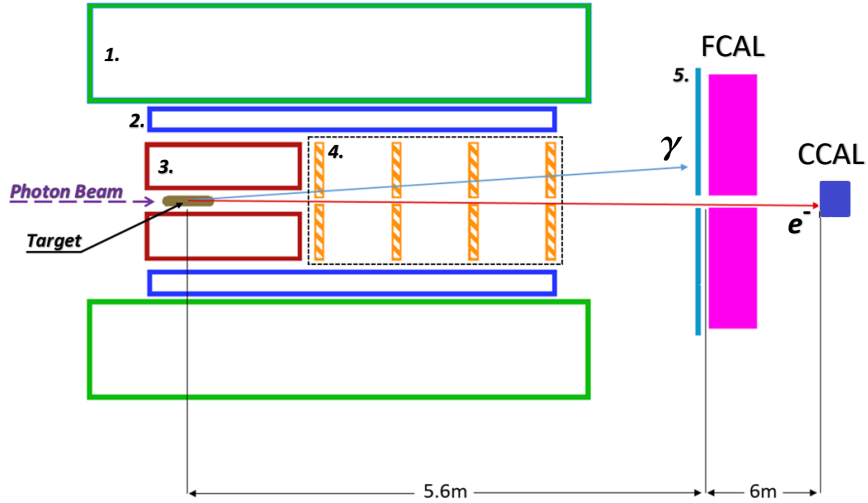


Figure 1: Schematic layout of the GlueX detector (not to scale). Numbers represent the following detector components: solenoid magnet (1), barrel calorimeter (2), central drift chamber (3), forward drift chambers (4), time-of-flight wall (5).

56 m long dipole magnet operated at a field of ~ 1.5 T and registered in the tagging scin-
 57 tillator counters. Each counter corresponds to the specific energy of the reconstructed
 58 electron. The tagging detectors span the beam photon energy range between 25% and
 59 98% of the electron beam energy and cover the range between 2.8 GeV and 11.0 GeV
 60 during the PrimEx- η experiment ². The typical energy resolution of the beam photon is
 61 about 0.1%. The photon beam propagates toward the GlueX target. A schematic view
 62 of the GlueX detector is illustrated in Fig. 1 ³.

63 The physics goal of the PrimEx- η experiment is to perform a precision measure-

²The electron beam energy during most production PrimEx- η runs was 11.2 GeV.

³Not shown on this plot is the DIRC detector, which was installed after the PrimEx- η experiment and is used for the particle identification in the forward direction.

64 ment of the $\eta \rightarrow \gamma\gamma$ decay width. The measurement will provide an important test
65 of quantum chromodynamics symmetries and is essential for the determination of fun-
66 damental properties such as the ratios of the light quark masses and the η - η' mixing
67 angle. The decay width will be extracted from the measurement of the photoproduc-
68 tion cross section of η mesons in the Coulomb field of a nucleus, which is known as the
69 Primakoff effect. The η mesons will be reconstructed by detecting two decay photons
70 in the forward calorimeter of the GlueX detector.

71 The cross section will be normalized using the Compton scattering process, which
72 will also be used to monitor the luminosity and control the detector stability during
73 data taking. Electrons and photons originating from Compton events in the target are
74 produced at small angles, typically outside the acceptance of the FCAL. In order to im-
75 prove the particles reconstruction in the forward direction, we built a small Compton
76 calorimeter consisting of 140 lead tungstate scintillating crystals. The CCAL was po-
77 sitioned about 6 m downstream from the FCAL as shown in Fig. 1. The CCAL covers
78 the polar angle range θ between 0.19° to 0.47° .

79 The PrimEx- η experiment started collecting data in the spring of 2019 and has
80 acquired 30% of the required statistics. During the experiment, the magnetic field
81 of the solenoid magnet was switched off in order to allow reconstruction of Compton
82 events. The photon flux was about $5 \cdot 10^6$ γ /sec (about five times lower than the nominal
83 GlueX flux) in the beam energy range of interest between 9.5 GeV and 11.6 GeV.

84 **3. Compton calorimeter of the PrimEx- η experiment**

85 *3.1. Calorimeter design*

86 The calorimeter design is shown in Fig. 2. The CCAL comprises an array of 12×12
87 lead tungstate modules with a 2×2 hole in the middle for the passage of the photon
88 beam. The modules are positioned inside a light tight box. A tungsten absorber is
89 placed in front of the innermost layer closest to the beamline to provide protection from
90 the high rate of particles predominantly originating from electromagnetic interactions.

91 The light yield from PbWO_4 crystals depends on temperature and decreases at
92 higher temperatures with a typical coefficient of $2\%/^\circ\text{C}$ at room temperature. Main-

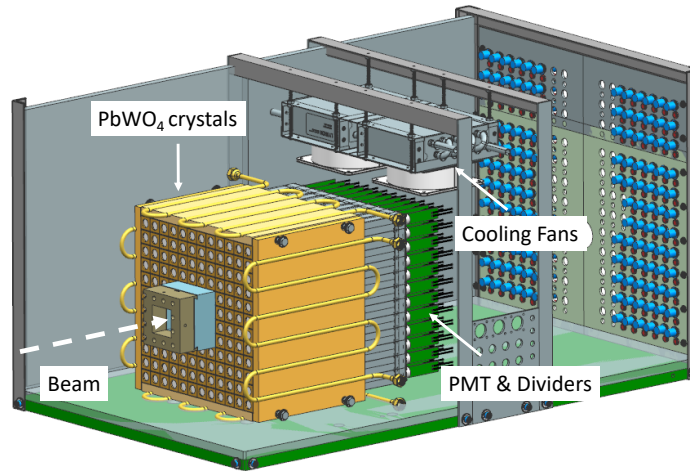


Figure 2: Schematic layout of the Compton calorimeter.

93 taining constant temperature is essential for the calorimeter operation. The calorimeter
94 modules are surrounded by four copper plates with built-in pipes to circulate a cooling
95 liquid and provide temperature stabilization. Foam insulation surrounds the detector
96 box. In order to prevent condensation, a nitrogen purge is applied. Two fans with a
97 water-based cooling system including radiators are installed on the top of the crystal
98 assembly to improve nitrogen circulation and heat dissipation from the PMT dividers.
99 The temperature was monitored and recorded during the experiment by five thermo-
100 couples attached to different points of the PbWO₄ module assembly. During the exper-
101 iment the temperature was maintained at $17^{\circ} \pm 0.2^{\circ}C$. The typical heat released by the
102 photomultiplier tube dividers of the whole detector was equivalent to about 30 Watts.
103 The detector was positioned on a platform, which allowed to move it in the vertical
104 and horizontal directions, perpendicular to the beam. The platform was remotely con-
105 trolled and provided a position accuracy of about $200 \mu m$. During detector calibration
106 each module was moved into the beam. The detector calibration will be discussed in
107 Section 3.5.

108 3.2. Module design

109 The design of the PbWO_4 module is based on the HyCal calorimeter, which was
110 used in several experiments in Jefferson Lab Hall B [17, 18]. An assembled calorime-
111 ter module is presented in Fig. 3. Each lead tungstate crystal is wrapped with a $60\ \mu\text{m}$
112 polymer Enhanced Specular Reflector film (ESR) manufactured by 3MTM, which al-
113 lows 98.5% reflectivity across the visible spectrum. In order to improve optical isola-
114 tion of each module from its neighbors, each crystal is wrapped with a layer of $25\ \mu\text{m}$
115 thick Tedlar. The PMT is located inside a G-10 fiberglass housing at the rear end of the
116 crystal. Two flanges are positioned at the crystal and housing ends and are connected
117 together using $25\ \mu\text{m}$ brass straps, which are brazed to the sides of the flanges. Four
118 set screws are pressed to the PMT housing flange to generate tension in the straps and
119 hold the assembly together. Light from the crystal is detected using a ten-stage Hama-
120 matsu PMT 4125, which is inserted into the housing and is coupled to the crystal using
121 optical grease (EJ-550) produced by Eljen Technology [19]. The PMT diameter is 19
122 mm. The PMT is pushed towards the crystal by using a G-10 retaining plate attached
123 to the back of the PMT with four tension screws connected to the PMT flange. The
124 PMT is instrumented with a high-voltage (HV) divider and amplifier positioned on the
125 same printed circuit board attached to the PMT socket.

126 3.3. Electronics

127 The PMT of each calorimeter module are equipped with an active base proto-
128 type [20], which was designed for the Neutral Particle Spectrometer in experimental
129 Hall C. The base combines a voltage divider and an amplifier powered by the current
130 flowing through the divider. The active base allowed the operation of the PMT at lower
131 voltage and consequently at lower anode current, which improves the detector rate ca-
132 pability and prolongs the PMT's life. The original Hamamatsu divider for this type of
133 PMT was modified by adding two bipolar transistors on the last two dynodes, which
134 provided gain stabilization at high rate. The active base had a relatively large amplifica-
135 tion of about a factor of 24 due to the large PMT count rate predicted by Monte Carlo
136 simulation of the NPS detector. Large amplification was not needed for the planned
137 run conditions of the PrimEx- η experiment. However, we subsequently used CCAL

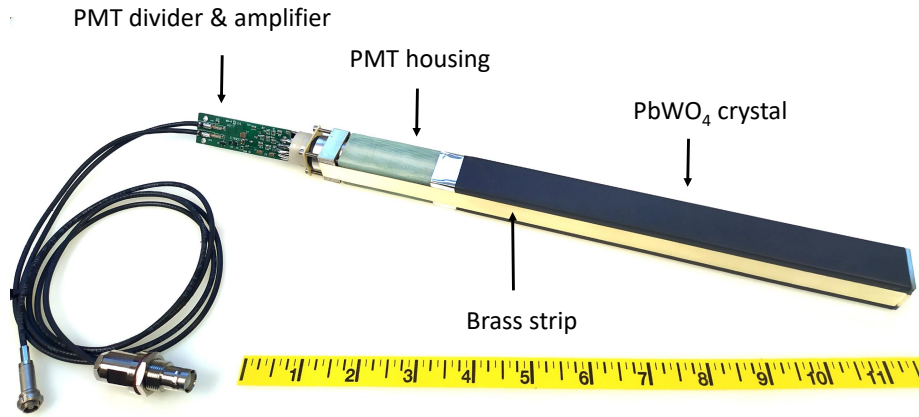


Figure 3: Calorimeter module showing main components: the PbWO_4 crystal, PMT housing, PMT divider, and signal and high-voltage cables.

138 in GlueX runs at significantly larger luminosity in order to study run conditions of the
 139 FCAL lead tungstate insert, where the amplifier will be required. This will be dis-
 140 cussed in Section 4.0.3. During the PrimEx run, the CCAL PMTs were operated at
 141 about 680 V, which produced a divider current of $260 \mu\text{A}$. The high voltage for each
 142 PMT was supplied by a 24-channel CAEN A7236SN module positioned in a SY4527
 143 mainframe.

144 Amplified PMT signals were digitized using a twelve-bit 16-channel flash ADCs
 145 electronics module operated at a sampling rate of 250 MHz. The ADC was designed
 146 at Jefferson Lab [21] and is used for the readout of several sub-detectors of the GlueX
 147 detector. The Field-Programmable Gate Array (FPGA) chip inside the ADC module
 148 allows the implementation of various programmable data processing algorithms for the
 149 trigger and readout. An example of a flash ADC signal pulse obtained from a calorime-
 150 ter module is shown in Fig. 4. In this example, the ADC was operated in the raw readout
 151 mode, where digitized amplitudes were read out for 100 samples, corresponding to the
 152 read out window size of 400 ns. During the PrimEx- η experiment, the ADC performed
 153 on-board integration of signal pulses, which amplitudes were above a threshold of 24

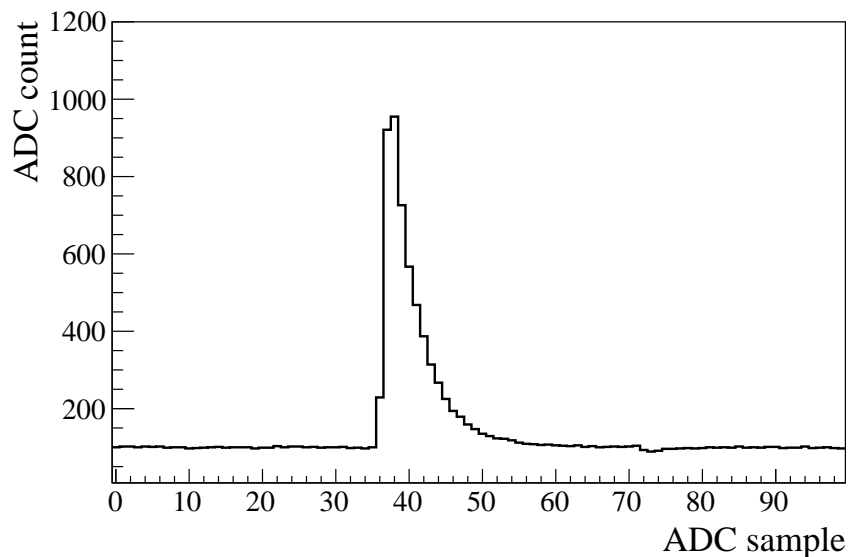


Figure 4: A typical flash ADC signal pulse obtained from a PbWO₄ module.

154 MeV. Amplitudes were summed in a time window of 64 ns and read out from the ADC
 155 module along with other parameters such as the pulse peak amplitude, pulse time, and
 156 data processing quality factors. This readout mode allowed to significantly reduce the
 157 data size and ADC readout time, and therefore did not induce any dead time in the data
 158 acquisition.

159 CCAL flash ADCs were positioned in a VXS (ANSI/VITA 41.0 standard) crate.
 160 VXS crates are used to host all readout electronics of the GlueX experiment. In ad-
 161 dition to the VME-bus used to read out data from electronics modules, the VXS is
 162 instrumented with a high-speed serial bus in order to increase the bandwidth to several
 163 Gb/sec and provide an interconnected network between modules. The bus is used to
 164 transmit amplitudes digitized by the ADC to trigger electronics modules to include the
 165 CCAL in the Level 1 trigger system of the GlueX detector.

166 3.4. Light Monitoring System

167 To monitor performance of each calorimeter channel, we designed an LED-based
 168 light monitoring system (LMS). The LMS optics includes a blue LED, a spherical lens

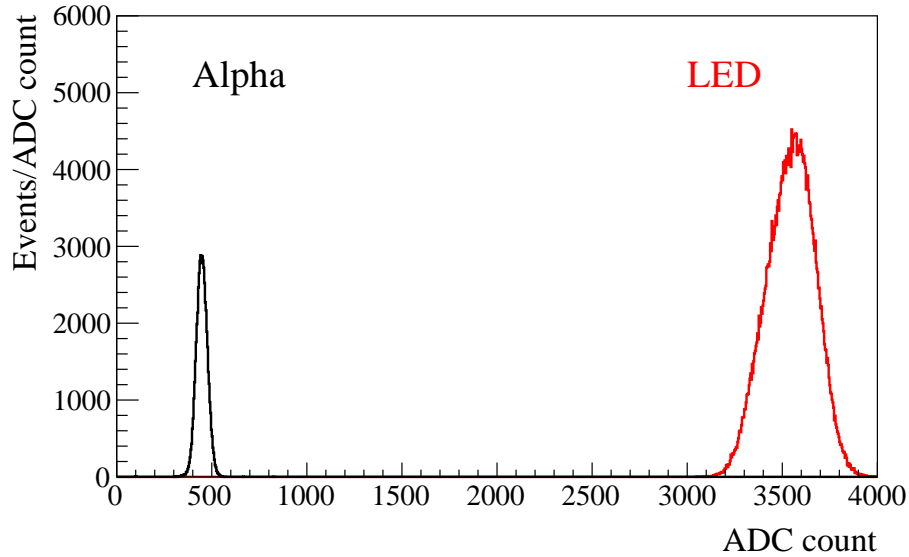


Figure 5: Flash ADC signal amplitudes induced by the LED and α -source in the reference PMT.

169 to correct the conical dispersion of the LED, and a diffusion grating to homogeneously
 170 mix the light. Light produced by the LED is incident on a bundle of plastic optical
 171 fibers (Edmund Optics) with a core diameter of $250\ \mu\text{m}$. Each fiber distributes light
 172 to an individual calorimeter module. On the crystal end, the fiber is attached to the
 173 module using a small acrylic cap glued to the crystal with a hole drilled through each
 174 cap to hold the fiber inside.

175 To monitor stability of the LED, we used two reference Hamamatsu 4125 PMTs,
 176 the same type as in the CCAL detector. Each PMT receives light from two sources: a
 177 single fiber from the LED and a YAP:Ce pulser unit, both glued to the PMT face. The
 178 pulser unit consists of a 0.15 mm thick YAP:Ce scintillation crystal with a diameter of
 179 3 mm spot activated by an ^{241}Am α source. The α source is used to monitor stability of
 180 the LED. The PMT is read out using a flash ADC. The high voltage on each reference
 181 PMT is adjusted to have the signals from both the LED and α source fit within the
 182 range of a 12-bit flash ADC corresponding to 4096 counts, as shown in Fig. 5. Each
 183 LED is driven by a CAEN 1495 module, which allows to generate LED pulses with a

184 programmable rate. The width of a signal pulse induced by the LED corresponds to
185 about 80% of the pulse width produced by the PbWO_4 scintillating crystal. The typical
186 amount of light injected by the LED to the crystal is equivalent to that emitted by 500
187 MeV photons.

188 The LMS was integrated into the GlueX trigger system and provided a special
189 trigger type during data taking. The LMS was extensively used during the detector
190 commissioning and injected light to the CCAL detector with a typical frequency of
191 100 Hz continuously during the PrimEx- η experiment. This LED rate was similar to
192 the trigger rate of events produced by the reference α source.

193 Most LMS components were positioned inside the temperature-stabilized detector
194 box. The stability of the LED system measured using the reference PMTs during the
195 entire PrimEx run was on the level of 1%. The ratio of signal ADC amplitudes from
196 the LED pulser to the α source obtained during different run periods of the 48-day
197 long PrimEx- η experiment is presented in Fig. 6. The ratio is normalized to the data in
198 the beginning of the experiment. Stability of most CCAL modules observed using the
199 LMS during about 1.5 months of the experiment was better than 6%. We did not apply
200 any PMT gain adjustments during the experiment.

201 3.5. Calibration

202 The energy calibration of the CCAL was performed by moving the calorimeter plat-
203 form and positioning each module into the photon beam during special low-intensity
204 calibration runs; these were called snake scans. The maximum rate observed in the
205 module exposed to the beam did not exceed 200 kHz at a threshold of 15 MeV. The
206 energy of each beam photon was determined by detecting a bremsstrahlung electron
207 using the GlueX tagging detectors described in Section 2. The tagging detectors cov-
208 ered the energy range of the photon beam between 2.8 GeV and 11 GeV. The spot size
209 of the collimated beam had a diameter of about 6 mm.

210 The calibration procedure was organized into several steps. First, we adjusted HVs
211 in the CCAL in order to equalize the energy response in the calorimeter modules for
212 the given beam energy, and set the maximum signal pulse amplitude to the appropriate
213 range of the flash ADC. We performed a snake scan, where the center of each module

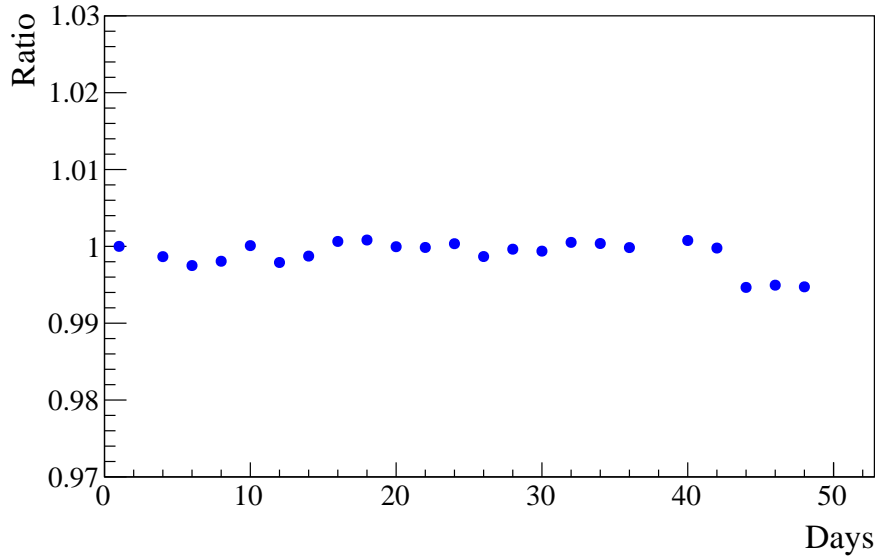


Figure 6: Ratio of signal ADC amplitudes from the LED pulser to the α -source measured by the reference PMT during different run periods of the 48-day long PrimEx- η experiment. The ratio is normalized to data in the beginning of the run.

214 was sequentially placed into the beam. The signal pulse amplitudes were measured
 215 for that module. No shower reconstruction was done at this stage. An example of
 216 the signal amplitude in the calorimeter module in units of the flash ADC counts as a
 217 function of the beam energy is presented in Fig. 7. The PMT voltage was tuned to set
 218 the amplitude induced by 11 GeV photons to 3500 ADC counts (which corresponds to
 219 1.7 V).

220 After adjusting voltages we repeated the snake scan and acquired data for the gain
 221 calibration. In the calibration we reconstructed showers in the calorimeter modules and
 222 constrained the reconstructed energy to the known beam energy. During shower recon-
 223 struction, energies from all modules constituting the shower were essentially summed
 224 up to the shower energy. For the CCAL shower reconstruction we adopted the algo-
 225 rithm which was originally used in the HyCal calorimeter [17] in JLab's experimental
 226 Hall B. The central part of the HyCal consists of the same type of crystals as those
 227 which we use in the CCAL. The gain of the central module in the shower, which was

228 exposed to the beam was corrected as follows:

$$G_C = G_I \cdot \frac{E_{\text{Shower}}}{E_{\text{Beam}}}, \quad (1)$$

229 where G_I is the initial gain of the module before the correction, G_C is the corrected
230 gain, E_{Shower} is the energy of the reconstructed electromagnetic shower, and E_{Beam} is
231 the beam energy. For calibration, we used a constant beam energy of 4.5 GeV. The gain
232 correction procedure was sequentially performed for all calorimeter modules, which
233 were inserted into the beam. In order to account for shower leakage in the inner and
234 outer layers of the calorimeter, the shower energy was adjusted in the reconstruction
235 program. The energy leakage was computed and corrected for by using a shape of the
236 shower profile. The calibration required a few iterations over all calorimeter modules.

237 The next step in the calibration was to determine corrections to the energy of recon-
238 structed showers, which had to be applied in order to account for non-linear calorimeter
239 responses due to readout energy thresholds, non linearity of the PMT and electronics,
240 and shower leakage. In the CCAL reconstruction, the shower energy was corrected
241 using a power function:

$$F(E) = P_0 \cdot E^{P_1 + P_2 \cdot E + P_3 \cdot E^2}, \quad (2)$$

242 where E corresponds to the initial shower energy before the correction, and the con-
243 stants, P , were obtained from the calibration. The shower energy correction was ap-
244 plied using calibration coefficients, P , corresponding to the shower module with the
245 largest energy deposition. The parameters, P , were determined for each CCAL module
246 individually using the snake scan data from a fit of the dependence of the reconstructed
247 shower energy on the beam energy to the correction function in Eq. 2. The typical
248 non-linear energy corrections to CCAL showers are 1 – 2% for the energies larger than
249 3 GeV, and 5 – 7% for 1 GeV showers. The relatively large correction required at small
250 energies can be explained by a non-linear response of the PMT amplifier and the flash
251 ADC readout threshold.

252 The CCAL calibration using the snake scans was performed in the beginning of the
253 GlueX experiment. In order to account for some small drift of PMT gains on a level
254 a few percent during the experiment, we adjusted the gains of the CCAL modules in
255 data analysis using Compton scattering candidates. No corrections to the PMT's HVs

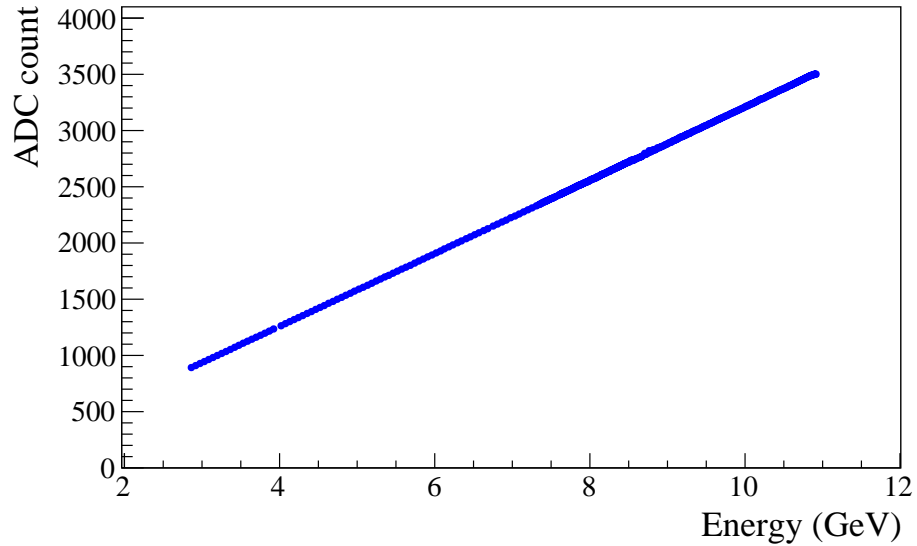


Figure 7: ADC signal pulse amplitude in the CCAL module as a function of the beam energy.

256 were applied during data taking. In the calibration, we made use of the fact that the
257 kinematics of the Compton scattering reaction is well defined. We selected showers in
258 the CCAL produced by Compton candidates and computed the expected energy of an
259 electron or photon, which initiated the shower, by using the shower's angle and known
260 beam energy. The gain calibration procedure was similar to that described in the snake
261 scan: the reconstructed and predicted energies of the shower were used to compute and
262 apply gain corrections. We compared the energy resolution of reconstructed Compton
263 candidates during different time periods of the PrimEx- η experiment, the difference
264 was found to be smaller than 2%.

265 We estimated the non-uniformity of the 140 CCAL modules by measuring the rel-
266 ative energy resolution for each individual module exposed to the beam. As the beam
267 can be positioned in the middle of each crystal with a good precision, better than
268 $200 \mu\text{m}$, the relative single-crystal energy resolution can characterize the uniformity
269 of the crystals used in the calorimeter. We measured the energy deposited by 6 GeV
270 photons in a single module and determined the energy resolution from a fit of the en-

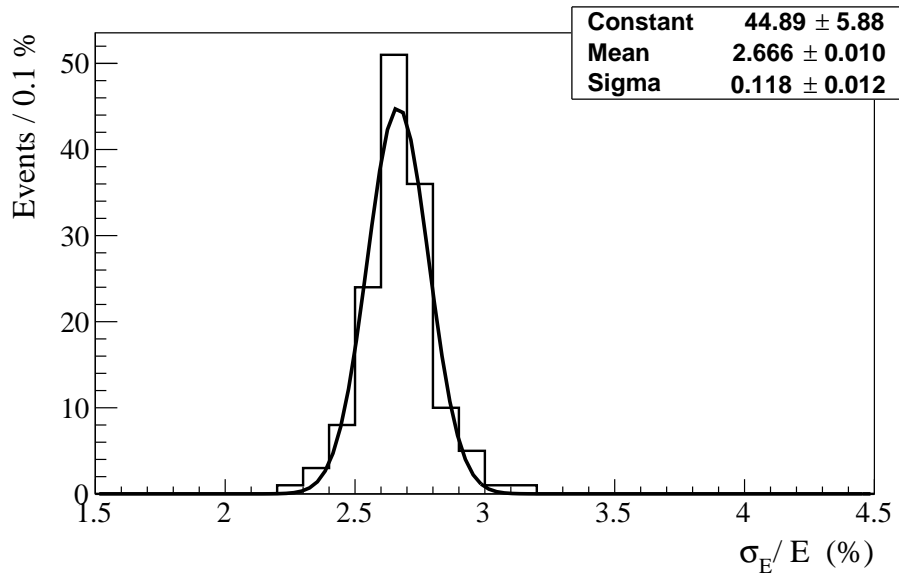


Figure 8: Relative energy resolution of 140 PbWO₄ modules installed on the CCAL measured with 6 GeV beam photons.

271 ergy distribution to a Crystal Ball function [22]. The relative energy resolution, defined
 272 as the width of the energy distribution divided to the average energy deposited in the
 273 module, obtained for all 140 CCAL modules is presented in Fig. 8. The distribution is
 274 fit to a Gaussian function. The non-uniformity of the modules, i.e., the spread of the
 275 distribution is found to be smaller than 5%.

276 During calibration, we observed some non-linearity of the PMT active base with the
 277 large amplification factor of 24, on the level of a few percent, which impacted both the
 278 pulse peak and pulse integral. The base performance became linear when the amplifier
 279 gain was reduced. In order to study the impact of the non-linearity on the detector
 280 energy resolution, we replaced the original PMT active bases for 9 CCAL modules (in
 281 the array of 3×3 modules) with modified bases where the amplifier was bypassed.
 282 After adjusting high voltages and re-calibrating PMT gains, we measured the energy
 283 resolution for different beam energies. The beam was incident on the center of the
 284 middle module in the array. An example of the energy deposited by 10 GeV photons is
 285 shown in Fig. 9. The energy resolution was obtained from a fit of the energy distribution

286 to a Crystal Ball function ⁴ implemented in the ROOT data analysis framework [22].
 287 The energy resolution as a function of the beam energy is shown in Fig. 10. The
 288 distribution was fit to the following function:

$$\frac{\sigma_E}{E} = \frac{S}{\sqrt{E}} \oplus \frac{N}{E} \oplus C, \quad (3)$$

289 where S represents the stochastic term, N the electronic noise and C the constant term,
 290 E is the beam energy in GeV, and the symbol \oplus indicates a quadratic sum. The fit
 291 yields: $S = (2.63 \pm 0.01)\%$, $N = (1.07 \pm 0.09)\%$, and $C = (0.53 \pm 0.01)\%$. The
 292 resolution was found to be about 10% better than that measured with the original base
 293 with the amplifier gain factor of 24 ⁵. We note, that the energy resolution depends on
 294 the energy thresholds, and is getting worse with the increase of the readout threshold.
 295 This dependence is stronger at small shower energies. For the ADC readout threshold
 296 of 15 MeV per crystal used in the analysis the expected relative degradation of the
 297 energy resolution in our energy range of interest is small and constitutes to about 1.3%
 298 for 2.8 GeV showers and much smaller than a percent for the shower energies around
 299 11 GeV. In the fit to the energy resolution, we did not account for the dependence on
 300 the readout threshold. The energy resolution decreases by 8% for 2.8 GeV photons
 301 if an energy threshold of 30 MeV is used. The energy resolution is consistent with
 302 that of the HyCal calorimeter [17], which was instrumented with crystals produced by
 303 SICCAS in 2001 and was used in several experiments in Jefferson Lab’s experimental
 304 Hall B. The HyCal PbWO₄ crystals have the same transverse size of 2.05 cm×2.05 cm,
 305 but a smaller length of 18 cm.

306 3.6. Performance during the PrimEx- η run

307 In the PrimEx- η experiment, we reconstructed Compton events produced by beam
 308 photons with the energy larger than 6 GeV. This energy range is covered by the GlueX
 309 pair spectrometer [23], which determines the photon flux needed for cross section
 310 measurements. An electron and photon produced in the Compton scattering process

⁴The function is named after the Crystal Ball collaboration.

⁵The linearity of the PMT active base is being currently improved; modified active bases will be installed before the new PrimEx- η run in 2021.

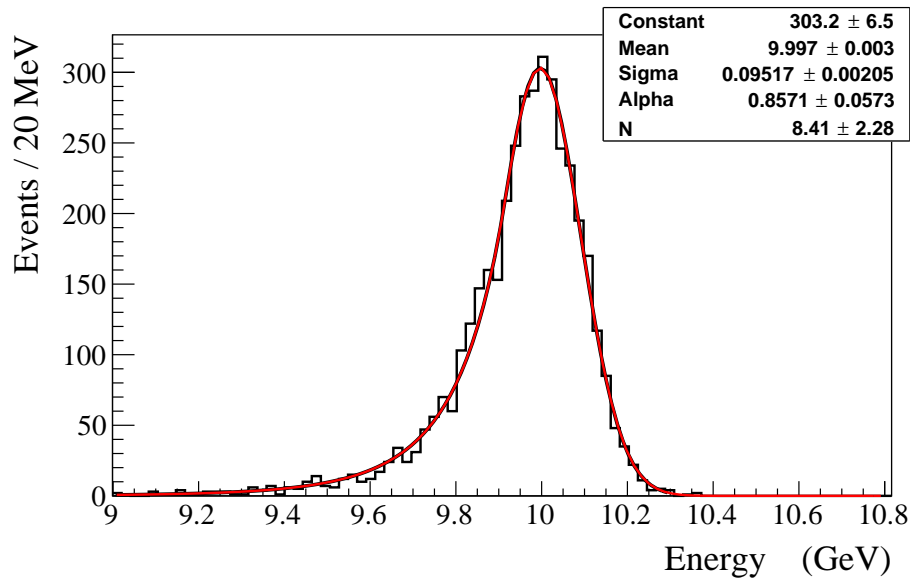


Figure 9: Energy distribution deposited by 10 GeV beam photons. The spectrum is fit to a Crystal Ball function.

311 were detected by reconstructing two showers, one in the FCAL and another one in
 312 the CCAL. The event topology of the reaction is such that the more energetic electron
 313 predominantly goes into the Compton calorimeter, while the photon strikes the FCAL.
 314 In order to accept Compton events during data taking and to reduce background orig-
 315 inating from low-energy electromagnetic and hadronic interactions, the CCAL was
 316 integrated to the Level 1 trigger system of the GlueX detector. The physics trigger was
 317 based on the total energy deposited in the forward and Compton calorimeters. The
 318 GlueX trigger is implemented on special-purpose programmable electronics modules
 319 with FPGA chips. The trigger architecture is described in Ref. [24]. The trigger rate
 320 as a function of the energy threshold is presented in Fig. 11. We collected data using a
 321 relatively small energy threshold of 3 GeV at a trigger rate of about 18 kHz. This rate
 322 did not produce any dead time in the data acquisition and trigger systems. The trigger
 323 rate is dominated by electromagnetic interactions, which was estimated using Geant
 324 detector simulation [25] and is superimposed on Fig. 11.

325 The typical rate in the CCAL modules measured during the experiment is presented

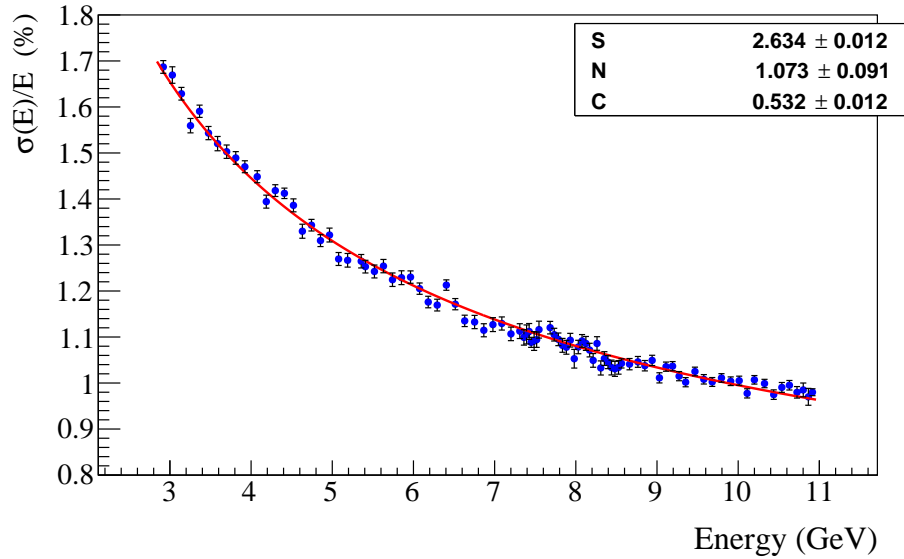


Figure 10: The CCAL energy resolution as a function of the photon energy.

326 in Fig. 12. In this plot, the photon beam goes through the center of the hole of 2×2
 327 modules in the middle of the detector. The rate was the largest in innermost detector
 328 layers closest to the beamline. The maximum rate in the PbWO_4 crystal was about 200
 329 kHz for an energy threshold of 30 MeV, which is equivalent to a signal pulse amplitude
 330 of 5 mV. This rate in the detector resulted in a negligibly small pile-up probability for
 331 the typical signal pulse width of 50 ns^6 . Before the experiment, we performed a high-
 332 rate performance study of the PMT and electronics using a laser and an LED periodic
 333 pulser and did not find any degradation of the PMT gain up to 2 MHz [26].

334 Timing resolution of reconstructed showers is an important characteristic of the
 335 detector performance. In the experiment we used timing information provided by the
 336 calorimeters to identify the accelerator beam bunch for which the interaction occurred
 337 in the detector and therefore related showers in the calorimeters with hits in the tagging
 338 detector, from the same event. A hit in the tagging detector defines the energy of the

⁶The pile-up effects can lead to the degradation of the energy resolution and have to be considered in the FCAL insert region closest to the beamline, where the rate will approach about 1 MHz per crystal.

339 beam photon. The time in the calorimeter module is provided by an algorithm imple-
 340 mented on the programmable FPGA chip of the flash ADC. The algorithm performs a
 341 search of the peak of the signal pulse and determines the time from the shape of the
 342 leading edge of the pulse. The times of all hits constituting the CCAL shower are com-
 343 bined to form the shower time by using an energy-weighted sum. The time difference
 344 between beam photon candidates and CCAL showers originating from Compton events
 345 is presented in Fig. 13. The main peak on this plot corresponds to beam photons and
 346 CCAL clusters produced in the same accelerator bunch. Satellite peaks, separated by
 347 the beam bunch period of about 4 ns, represent accidental beam photons from acceler-
 348 ator bunches not associated with the interaction in the detector. The dependence of the
 349 time resolution, σ_t , of CCAL showers on the shower energy can be parameterized by
 350 the following function: $\sigma_t = \frac{0.32 \text{ ns}}{\sqrt{E}} \oplus 0.09 \text{ ns}$, where E is the shower energy in units of
 351 GeV, the symbol \oplus denotes a quadratic sum, and the parameters were obtained from a
 352 fit to the data. The time resolution is improved with the increase of the shower energy
 353 and constitutes about 330 ps and 140 ps for 1 GeV and 9 GeV showers, respectively.
 354 In the PrimEx- η experiment the CCAL allowed a clear separation of beam photons
 355 originating from different beam bunches.

356 Reconstruction of electromagnetic showers in the FCAL is performed using an al-
 357 gorithm described in Ref. [27], which is a part of the standard GlueX reconstruction
 358 software. For the CCAL, we implemented an algorithm originally developed for the
 359 GAMS spectrometer [28, 29], which was subsequently adopted for the HyCal [17]
 360 in JLab's experimental Hall B. The algorithm was studied using Geant detector sim-
 361 ulation [25]. No visible bias in the reconstructed shower energy was observed after
 362 applying a non-linear energy correction. The shower coordinates were reconstructed
 363 by combining the positions of all modules constituting the shower and using a loga-
 364 rithmically energy-weighted sum. The coordinates of a reconstructed shower exhibit
 365 a small bias on the level of 0.1 - 0.2 mm, which depends on the position of the in-
 366 coming photon on the face of the crystal. The shower position resolution depends on
 367 the cluster energy and also correlates with the coordinate of the incident photon. The
 368 resolution is smaller near the edge of the crystal and increases at the crystal center.
 369 The typical position resolution of 4 GeV photons is 1.4 mm. The algorithm provides a

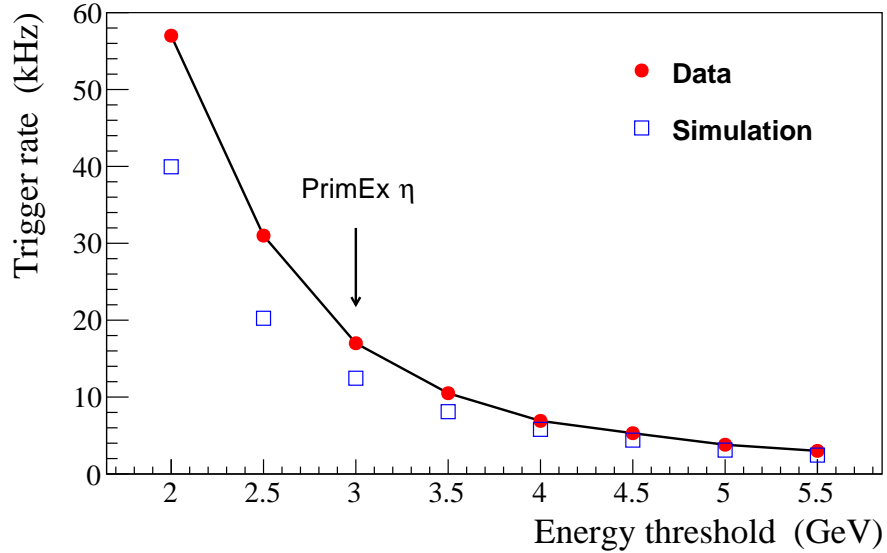


Figure 11: Trigger rate as a function of the total energy deposited in the FCAL and CCAL. Circles represent data and boxes represent the rate of electromagnetic interactions predicted by Monte Carlo simulation. The arrow indicates the energy threshold used in PrimEx- η production runs.

370 good separation of overlapping showers in the calorimeter by using profiles of electro-
 371 magnetic showers. Two photons with energies between 1 GeV and 5 GeV positioned
 372 at a distance of 4 cm from each other can be reconstructed with a typical efficiency
 373 larger than 80%. The average shower multiplicity per event in the CCAL is ~ 1.2 .
 374 We consider to use this algorithm to reconstruct showers in the FCAL insert, which
 375 will be operated at significantly larger luminosity. In the reconstruction of Compton
 376 candidates we made use of the well defined kinematics of the two-body reaction. We
 377 selected events with two reconstructed showers, one in the CCAL and another one in
 378 the FCAL, that originated from the same beam interaction. The time difference be-
 379 tween the showers and the beam photon was required to be smaller than 2 ns, which
 380 can be compared with the beam bunch period of 4 ns. We applied energy thresholds of
 381 0.5 GeV and 1 GeV for showers reconstructed in the FCAL and CCAL, respectively.
 382 The difference in the azimuthal angle between the reconstructed photon and electron
 383 was required to be $|\Delta\phi| < 5\sigma_\phi$, where $\sigma_\phi = 5.5^\circ$ is the angular resolution. For events

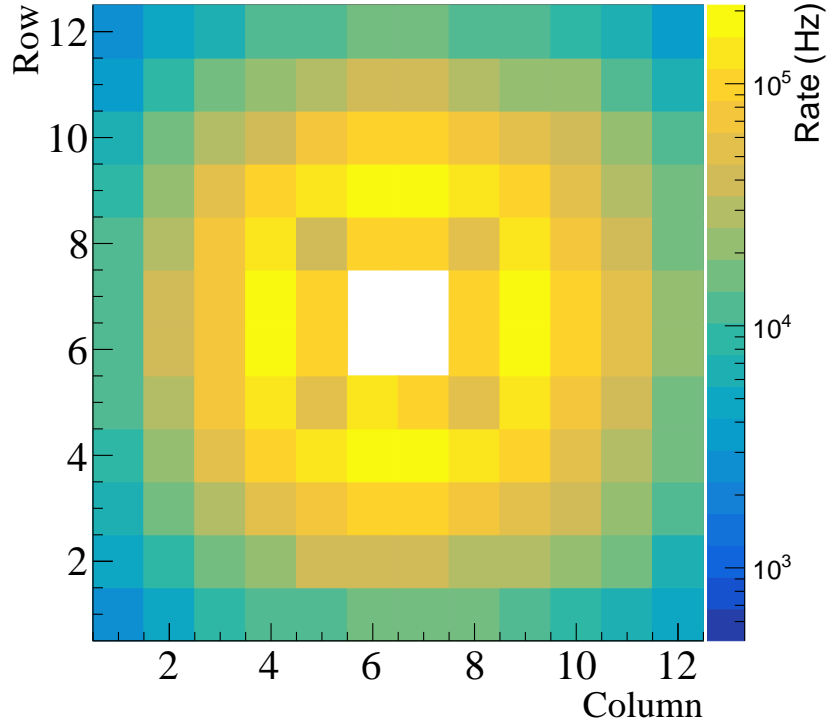


Figure 12: Rates in the CCAL modules during PrimEx- η production run. The energy threshold corresponds to 30 MeV. The beam goes through the center of the hole in the middle of the plot.

384 that passed the selection criteria we used the elasticity distribution, which is defined as
 385 the reconstructed energy in the event minus the beam energy. The elasticity distribu-
 386 tion for Compton candidates produced by beam photons in the energy range between 6
 387 GeV and 7 GeV is presented in Fig. 14. The distribution was fit to the sum of a Gaus-
 388 sian and a second order polynomial function. The energy resolution of reconstructed
 389 Compton candidates in this energy range is 125 MeV. The measured resolution was
 390 found to be in a good agreement, at a level of a few percent, with that predicted by
 391 the Monte Carlo simulation. In this plot, we subtracted background originating from
 392 accidental beam photons. This background was measured using off-time interactions
 393 and amounted to about 15%. The relatively small background, on the level of 10%,

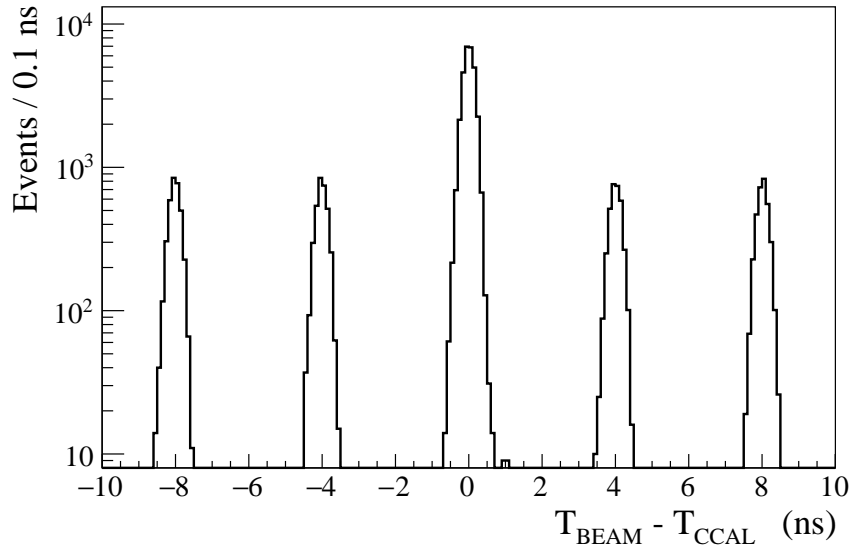


Figure 13: Time difference between beam photons and reconstructed CCAL showers for Compton candidates. Peaks are separated by the beam bunch period of 4 ns.

394 produced by interactions of the photon beam with the beamline material downstream
 395 the GlueX target was measured using empty-target runs and was also excluded from
 396 the elasticity distribution in Fig. 14. The small remaining background under the peak
 397 of the elasticity distribution originates from the pair production reaction. For the beam
 398 energy range of interest, the e^+e^- pairs are typically produced at small polar angles.
 399 The pair production contribution was estimated using the Geant simulation to be on the
 400 level of a few percent. The CCAL allowed to clearly reconstruct Compton candidates
 401 in the PrimEx- η experiment.

402 **4. Upgrade of the GlueX forward calorimeter**

403 The forward calorimeter of the GlueX detector consists of 2800 lead glass modules,
 404 each with a size of 4 cm \times 4 cm \times 45 cm, and is positioned about 6 m downstream
 405 of the target, as shown in Fig. 1. The FCAL covers a polar angle of photons produced
 406 from the target between 1° and 11° and detects showers with energies in the range of

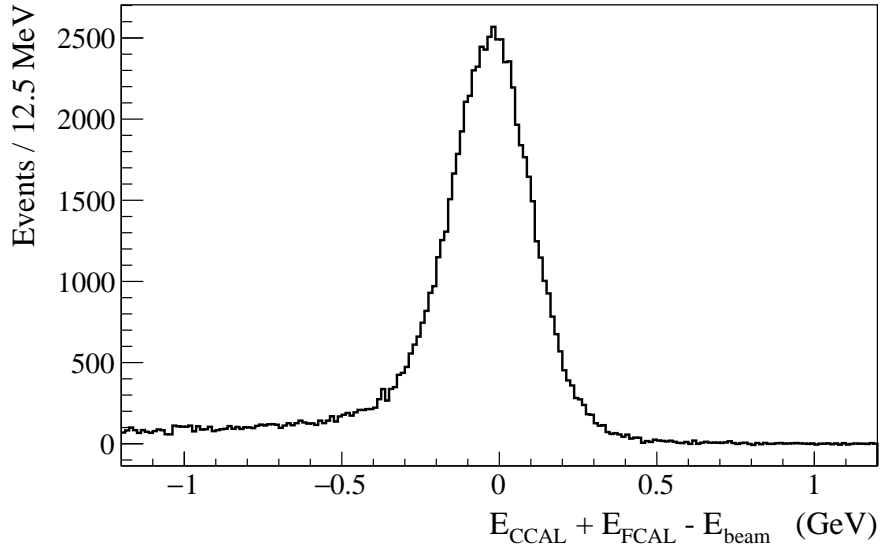


Figure 14: Elasticity distribution of reconstructed Compton candidates. The elasticity is defined as the energy of two clusters in the calorimeters minus the beam energy.

407 0.1 - 8 GeV. The Cherenkov light produced in the module is detected by FEU-84-3
 408 photomultiplier tubes, instrumented with Cockcroft-Walton bases [30]. The typical
 409 energy resolution of the FCAL is $\sigma_E/E = 6.2\%/\sqrt{E} \oplus 4.7\%$ [7].

410 The future physics program with the GlueX detector in Hall D will require an up-
 411 grade of the inner part of the forward calorimeter with high-granularity, high-resolution
 412 PbWO_4 crystals. The lead tungstate insert will improve the separation of clusters in the
 413 forward direction and the energy resolution of reconstructed photons by about a fac-
 414 tor of two. Lead tungstate crystals possess better radiation hardness compared to lead
 415 glass, which is important for the long term operation of the detector at high luminosity.
 416 The size of the insert will tentatively comprise 1596 PbWO_4 crystals, which will form
 417 an array of 40×40 modules⁷. Similar to the CCAL, the insert will have a beam hole
 418 of 2×2 modules and a tungsten absorber used to shield the detector layer closest to

⁷The insert size proposed for the JEF experiment [10] is 1 m \times 1 m; the actual size will depend on the availability of funds.

419 the beamline. A schematic view of the FCAL frame with the installed lead tungstate
420 insert is presented in Fig. 15. Due to the different size of the lead glass bars and lead
421 tungstate crystals, the lead glass modules stacked around the PbWO_4 insert will form
422 four regions with a relative offset between modules; those regions are shown in green
423 color in this plot.

424 The PbWO_4 module design of the FCAL insert will essentially be the same as for
425 the CCAL, except for some small modifications needed to handle the magnetic field
426 present in the FCAL region. The PMT housing made of the G-10 fiberglass mate-
427 rial will be replaced by a soft iron housing in order to reduce the magnetic field. The
428 housing length will be increased to extend the magnetic shield beyond the PMT pho-
429 tothode. An acrylic optical light guide will be inserted inside the PMT housing to
430 couple the crystal and PMT.

431 The upgraded FCAL will be operated in GlueX experiments using a 30 cm long
432 liquid hydrogen target at the designed photon flux of $5 \cdot 10^7 \gamma/\text{sec}$ in the energy range
433 between 8.4 GeV and 9 GeV. The designed luminosity is significantly larger than that
434 used in the PrimEx- η experiment and was achieved after the PrimEx run in the fall
435 of 2019. In order to finalize the design of the PMT electronics, it is important to
436 understand detector rates in the FCAL insert, especially in layers close to the beamline.
437 We used the CCAL during high-intensity GlueX runs to study run conditions for the
438 FCAL insert.

439 *4.0.1. Magnetic shielding of PMTs*

440 The longitudinal (directed along the beamline) and transverse (directed perpendic-
441 ular to the axis of the beamline) components of the magnetic field produced by the
442 GlueX solenoid magnet in the FCAL PbWO_4 insert area vary between 40 - 55 Gauss
443 and 0 - 9 Gauss, respectively. The longitudinal field is the largest on the beamline,
444 where the transverse component is practically absent. We studied the PMT magnetic
445 shielding using a prototype consisting of an array of 3×3 PMT iron housings made of
446 AISI 1020 steel, which was positioned in the middle of Helmholtz coils. Each housing
447 had a size of 20.6 mm \times 20.6 mm \times 104 mm with a 20 mm round hole in the middle
448 for the PMT. This corresponds to the realistic size of the magnetic shield that will be

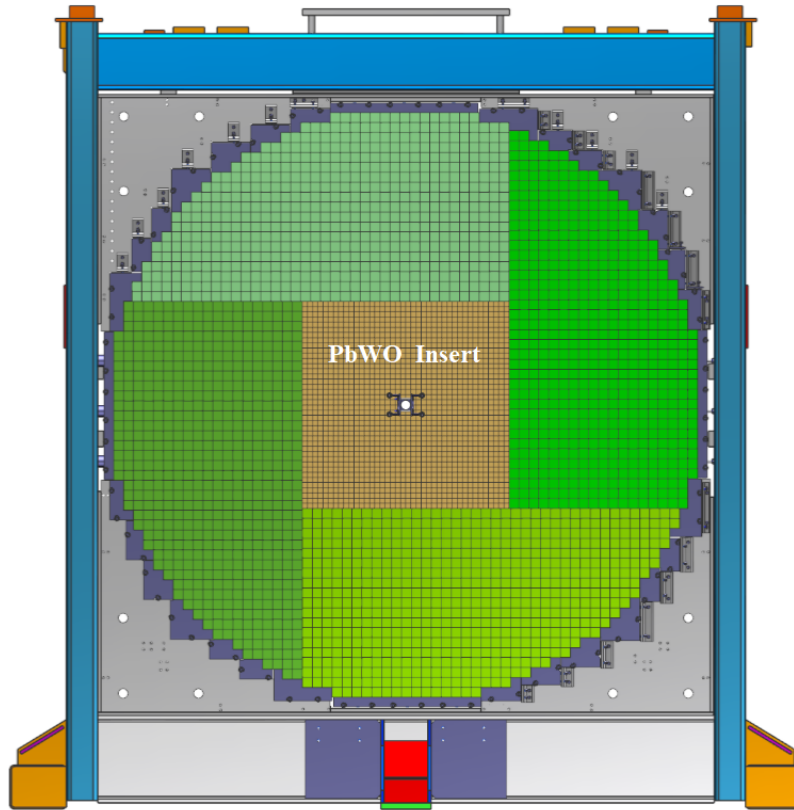


Figure 15: FCAL frame with calorimeter modules installed: PbWO_4 crystals (brown area), lead glass blocks (green). The photon beam passes through the hole in the middle of the calorimeter.

449 used in the calorimeter module assembly. Inside the housing we inserted two layers of
 450 mu-metal cylinders, with thicknesses of $350 \mu\text{m}$ and $50 \mu\text{m}$, separated from each other
 451 by a Kapton film. The thickest cylinder was spot welded and annealed.

452 The Helmholtz coils had a diameter of about 1.5 m and can generate a uniform
 453 magnetic field with variable strength below 100 Gauss. A Hall probe was inserted
 454 into the central module of the prototype to measure the magnetic field at different Z-
 455 positions along the length of the cylinder. The field was measured for two different
 456 orientations of the prototype with respect to the magnetic field: field oriented along the
 457 PMT (longitudinal, B_z) and perpendicular to the PMT housing (transverse, B_x). Field

458 measurements are presented in Fig. 16. The PMT shield significantly reduces both the
459 longitudinal and transverse fields to the level of $B_z \sim 1$ Gauss and $B_x \ll 1$ Gauss. The
460 transverse field, which is well shielded, is more critical for the PMT operation, as it
461 is directed perpendicular to the electron trajectory inside the photo tube and deflects
462 electrons, resulting in the degradation of the photon detector efficiency and gain. The
463 field reaches a plateau at $Z = 3$ cm from the face of the housing. We will use a 3.5
464 cm long acrylic light guide in order to position the PMT in the area with the smallest
465 magnetic field. The most sensitive to the magnetic field part of the PMT is a 4.6 cm long
466 region between the photocathode and the last dynode. The location of this region inside
467 the PMT shield housing is shown as a box in Fig. 16. The actual field inside the FCAL
468 insert module is expected to be even smaller due to the collective shielding effect, i.e.,
469 the large amount of shielding material installed on surrounding modules [31].

470 We studied performance of the shielded PMT in the magnetic field using an LED
471 pulser. A blue LED with a light diffuser was placed about 20 cm from the PMT housing
472 prototype and was aligned with the middle module. The PMT response was measured
473 for different pulse amplitudes and operational high voltages. In order to study the con-
474 tributions from longitudinal and transverse field components we rotated the prototype
475 by different angles. Signal amplitudes as a function of the magnetic field measured in
476 the prototype tilted by about 10 degrees are presented on the top plot of Fig. 17. Am-
477 plitudes, normalized to measurements without magnetic field, are shown on the bottom
478 plot. The relative degradation of the signal amplitude for the maximum field in the
479 FCAL insert region of $B = 55$ Gauss ($B_z \sim 54$ Gauss and $B_x \sim 9$ Gauss) was measured
480 to be on the level of 1%. The proposed shielding configuration is sufficient to reduce
481 the magnetic field to the level suitable for the PMT operation.

482 4.0.2. Light guide studies

483 Studies of the magnetic shielding demonstrated that the PMT has to be positioned
484 inside the iron housing at the distance of at least 3 cm from the face of the PbWO_4
485 crystal. In order to do this, in the FCAL insert module we use a 3.5 cm long acrylic
486 cylindrical light guide with a diameter of 18.5 mm between the PMT and the PbWO_4
487 crystal. The light guide is wrapped with reflective ESR foil and attached to the PMT

488 with Dymax 3094 UV curing glue. Optical coupling to the crystal is provided by a
489 “silicon cookie”: a 1 mm thick transparent rubber cylinder made of the room tempera-
490 ture vulcanized silicon compound, RTV615. The silicon cookie is not glued to the light
491 guide or the crystal, so the module can be easily disassembled if its PMT needs to be
492 replaced.

493 We compared light losses of the FCAL insert module instrumented with the light
494 guide with the CCAL module, where the PMT was coupled directly to the crystal using
495 an optical grease. Light collection was measured using electrons provided by the Hall
496 D pair spectrometer (PS) [23]. The PS is used to measure the flux of beam photons
497 delivered to the experimental hall by detecting electromagnetic electron-positron pairs
498 produced by the photons in a thin converter inserted to the beam. Leptons from the pair
499 are deflected in a dipole magnet and registered using scintillator detectors placed in the
500 electron and positron arms of the spectrometer. The energy of a lepton is detected using
501 a high-granularity PS hodoscope, which consists of 145 scintillating tiles and covers
502 the energy range between 3 GeV and 6 GeV. Each tile corresponds to the specific lepton
503 energy.

504 The relative light yield of the module with and without the light guide was estimated
505 by positioning the module behind the PS and measuring signal amplitudes induced by
506 the PS electrons. We first measured the ADC response in the CCAL module, which was
507 subsequently modified by adding the light guide to the same PMT and crystal and was
508 placed to the same spot of the PS test setup. Results of the measurements are presented
509 in Fig. 18. The ADC amplitude of the calorimeter module is presented as a function
510 of the PS tile for the two module configurations with and without the light guide. The
511 light guide results in a relatively small loss of light of 15 – 20% compared with the
512 CCAL module. We note that wrapping the light guide with the reflective material is
513 important. Losses in unwrapped light guide constitute about 35%. We repeated light
514 collection measurements using two more modules and obtained consistent results.

515 *4.0.3. Detector rate*

516 The PMT anode current is one of the critical characteristics that have to be consid-
517 ered during the design of the PMT divider. Typically the anode current should be on

518 the level of a few micro amperes and significantly smaller than the divider current in
519 order to provide stable performance of the PMT base and prevent the long-term degra-
520 dation of the PMT. Some lifetime tests of the Hamamatsu 4125 PMT are described in
521 Ref. [32].

522 The anode current (I) was measured in the CCAL modules during data production
523 runs at the GlueX nominal luminosity. It was obtained by measuring the average volt-
524 age in the flash ADC induced by particles incident on the CCAL module as follows:

$$I = \frac{\bar{U}}{R} \cdot \frac{1}{G}, \quad (4)$$

525 where \bar{U} is the average voltage in units of Volts, R is the input impedance of the am-
526 plifier ($\sim 50 \Omega$), and G is the amplifier gain of 24. A periodic pulser not associated
527 with an interaction in the detector was used as a trigger to read out flash ADC raw data
528 for each CCAL module in a time window of 400 ns. The voltage was determined by
529 summing up ADC amplitudes in the readout window and normalizing the sum to the
530 window size. The typical anode current measured in CCAL modules situated at differ-
531 ent distances from the beamline is presented in Fig. 19. Modules from the first CCAL
532 layer closest to the beamline and the outer most layer were not used in the analysis.
533 The inner modules were shielded by a tungsten absorber and the outer modules were
534 obscured by the FCAL. The rate in the detector is dominated by the forward-directed
535 electromagnetic background. The estimated anode current is the largest in the inner-
536 most layer of the detector closest to the beamline and amounts to about $1.4 \mu\text{A}$. This
537 current is significantly smaller than the PMT divider current of about $300 \mu\text{A}$.

538 We used the CCAL measurements to estimate the current in the FCAL insert. Tak-
539 ing the geometrical location of FCAL and CCAL modules into account, the largest
540 PMT current in the FCAL insert modules closest to the beamline and not shielded by
541 the absorber was conservatively estimated to be about $15 \mu\text{A}$. We assume that the PMT
542 base is operated at 1 kV and no amplifier is used. The detector rate drops rapidly with
543 the increase of the radial distance from the beamline. The estimated anode current is
544 relatively large and must be reduced by lowering the PMT high voltage. We are con-
545 sidering to instrument PMTs in a few inner FCAL insert layers with an amplifier with a
546 gain of 5 and to omit the amplifier on other modules. We are planning to perform more

547 beam tests of the FCAL insert active base using the CCAL in forthcoming GlueX runs
548 in 2021 - 2022.

549 **5. Neutral Particle Spectrometer**

550 The NPS is a new facility in Hall C that will allow access to precision measurements
551 of small cross sections of reactions with neutral final states. The NPS consists of an
552 electromagnetic calorimeter preceded by a sweeping magnet. As operated in Hall C, it
553 replaces one of the focusing spectrometers.

554 The NPS science program currently features six fully approved experiments. E12-
555 13-010 [11] and E12-06-114 [12] experiments will measure the Exclusive Deeply Vir-
556 tual Compton Scattering and π^0 cross sections to the highest Q^2 accessible at Jefferson
557 Lab. Both experiments will provide important information for understanding General-
558 ized Parton Distributions (GPDs). The E12-13-007 [13] experiment will study semi-
559 inclusive π^0 electroproduction process and seek to improve our understanding of the
560 factorization framework, which is important for 12 GeV Jefferson Lab semi-inclusive
561 deep-inelastic scattering program. Measurements of Wide-Angle and Timelike Comp-
562 ton Scattering reactions will be performed by the E12-14-003 [14] and E12-17-008 [15]
563 experiments. These measurements will allow to test universality of GPDs using high-
564 energy photon beams. The NPS will also be used in the E12-14-005 [16] experiment to
565 study exclusive production of π^0 at large momentum transfers in the process $\gamma p \rightarrow \pi^0 p$.

566 The NPS science program requires neutral particle detection over an angular range
567 between 6 and 57.3 degrees at distances of between 3 and 11 meters ⁸ from the exper-
568 imental target. The experiments will use a high-intensity beam of electrons with the
569 energies of 6.6, 8.8, and 11 GeV, and a typical luminosity of $\sim 10^{38}$ cm⁻²s⁻¹ as well
570 as a secondary beam of photons incident on a liquid hydrogen target. A vertical-bend
571 sweeping magnet with integrated field strength of 0.3 Tm will be installed in front of
572 the spectrometer in order to suppress and eliminate background of charged particle
573 tracks originating from the target. The photon detection is the limiting factor of the ex-

⁸The minimum NPS angle at 3 m is 8.5 degrees; at 4 m it is 6 degrees.

574 periments. Exclusivity of the reaction is ensured by the missing mass technique and the
575 missing-mass resolution is dominated by the energy resolution of the calorimeter. The
576 calorimeter is anticipated to provide the spacial resolution of 2-3 mm and the energy
577 resolution of about $2.5\%/\sqrt{E}$. The NPS consists of 1080 PbWO_4 crystals that form
578 an array of 30×36 modules. Similarly to the FCAL insert in Hall D, the NPS will be
579 built from the crystals of the same size, and instrumented with the same type of PMTs
580 and readout electronics. The details of the mechanical assembly and commissioning
581 of the NPS are currently under development and will be described in a forthcoming
582 publication.

583 The radiation hardness and good optical quality of lead tungstate crystals are critical
584 for the NPS calorimeter. The NPS collaboration, in a synergistic effort with the EIC
585 eRD1 consortium, has characterized to date over 1200 PbWO_4 crystals produced by
586 CRYTUR and SICCAS from 2014 to the present. The results of these studies have
587 been published in Ref. [33]. CRYTUR crystal samples were found to have greater
588 overall uniformity in transmittance and light yield, and better radiation hardness. Of
589 the samples characterized by the NPS collaboration 140 SICCAS crystals have been
590 used in the CCAL detector.

591 **6. Summary**

592 We described the design and performance of the Compton CALorimeter (CCAL),
593 which was constructed using 140 lead tungstate PbWO_4 crystals recently produced by
594 SICCAS. The calorimeter was successfully used in the PrimEx- η experiment in spring
595 of 2019 for reconstruction of Compton scattering events. The CCAL served as a pro-
596 totype for two large-scale electromagnetic calorimeters based on the PbWO_4 crystals:
597 the lead tungstate insert of the Forward CALorimeter (FCAL) of the GlueX detector
598 and the Neutral Particle Spectrometer (NPS). Experience gained during construction
599 and operation of the CCAL provided important information for finalizing the design
600 of FCAL PbWO_4 modules and understanding the performance of PMT dividers and
601 also served to further optimize the NPS calorimeter. We anticipate to use the CCAL in
602 forthcoming GlueX runs in 2021 - 2022 to perform final tests of the PMT dividers for

603 the FCAL insert. We presented the design of the FCAL lead tungstate insert and gave
604 an overview of the NPS project.

605 **7. Acknowledgments**

606 This work was supported by the Department of Energy. Jefferson Science Asso-
607 ciates, LLC operated Thomas Jefferson National Accelerator Facility for the United
608 States Department of Energy under contract DE-AC05-06OR23177. This work was
609 supported in part by NSF grants PHY-1714133, PHY-2012430 and PHY-1812396, and
610 the U.S. Department of Energy Grant DE-FG02-03ER41231. We thank the NPS col-
611 laboration/project for providing PbWO_4 crystals and PMTs used in the construction of
612 the CCAL.

613 **References**

- 614 [1] P. Adzic, et al., Results of the first performance tests of the CMS electromag-
615 netic calorimeter, *Eur. Phys. J. C* 44S1 (2006) 1–10. doi:[10.1140/epjcd/
616 s2005-02-011-3](https://doi.org/10.1140/epjcd/s2005-02-011-3).
- 617 [2] D. D.V. Aleksandrov, et al., A high resolution electromagnetic calorimeter based
618 on lead-tungstate crystals, *Nuclear Instruments and Methods in Physics Research*
619 *Section A: Accelerators, Spectrometers, Detectors and Associated Equipment*
620 550 (1) (2005) 169–184. doi:[https://doi.org/10.1016/j.nima.2005.
621 03.174](https://doi.org/10.1016/j.nima.2005.03.174).
- 622 [3] M. Kavatsyuk, et al., Performance of the prototype of the electromagnetic
623 calorimeter for panda, *Nuclear Instruments and Methods in Physics Research*
624 *Section A: Accelerators, Spectrometers, Detectors and Associated Equipment*
625 648 (1) (2011) 77–91. doi:[https://doi.org/10.1016/j.nima.2011.06.
626 044](https://doi.org/10.1016/j.nima.2011.06.044).
- 627 [4] I. Balossino, et al., The hps electromagnetic calorimeter, *Nuclear Instruments*
628 *and Methods in Physics Research Section A: Accelerators, Spectrometers, De-*

- 629 tectors and Associated Equipment 854 (2017) 89–99. doi:[https://doi.org/](https://doi.org/10.1016/j.nima.2017.02.065)
630 [10.1016/j.nima.2017.02.065](https://doi.org/10.1016/j.nima.2017.02.065).
- 631 [5] A. Acker, et al., The clas12 forward tagger, Nuclear Instruments and Methods
632 in Physics Research Section A: Accelerators, Spectrometers, Detectors and As-
633 sociated Equipment 959 (2020) 163475. doi:[https://doi.org/10.1016/j.](https://doi.org/10.1016/j.nima.2020.163475)
634 [nima.2020.163475](https://doi.org/10.1016/j.nima.2020.163475).
- 635 [6] JLab Experiment **E12-10-011**, A Precision Measurement of the η Radiative De-
636 cay Width via the Primakoff Effect, available online: [https://www.jlab.org/](https://www.jlab.org/exp_prog/proposals/10/PR12-10-011.pdf)
637 [exp_prog/proposals/10/PR12-10-011.pdf](https://www.jlab.org/exp_prog/proposals/10/PR12-10-011.pdf).
- 638 [7] S. Adhikari, et al., The GLUEX beamline and detector, Nucl. Instrum. Meth.
639 A 987 (2021) 164807. arXiv:2005.14272, doi:[10.1016/j.nima.2020.](https://doi.org/10.1016/j.nima.2020.164807)
640 [164807](https://doi.org/10.1016/j.nima.2020.164807).
- 641 [8] T. Horn, et al., Scintillating crystals for the Neutral Particle Spectrometer in Hall
642 C at JLab, Nucl. Instrum. Meth. A 956 (2020) 163375. arXiv:1911.11577,
643 doi:[10.1016/j.nima.2019.163375](https://doi.org/10.1016/j.nima.2019.163375).
- 644 [9] R. Abdul Khalek, et al., Science Requirements and Detector Concepts for the
645 Electron-Ion Collider: EIC Yellow Report arXiv:2103.05419.
- 646 [10] JLab Experiment **E12-12-002**, Eta Decays with Emphasis on Rare Neutral
647 Modes: The JLab Eta Factory (JEF) Experiment, available online: [https://www.](https://www.jlab.org/exp_prog/proposals/14/PR12-14-004.pdf)
648 [jlab.org/exp_prog/proposals/14/PR12-14-004.pdf](https://www.jlab.org/exp_prog/proposals/14/PR12-14-004.pdf).
- 649 [11] JLab experiment **E12-13-010**, Exclusive Deeply Virtual Compton and Neutral
650 Pion Cross-Section Measurements in Hall C, available online: [https://www.](https://www.jlab.org/exp_prog/proposals/13/PR12-13-010.pdf)
651 [jlab.org/exp_prog/proposals/13/PR12-13-010.pdf](https://www.jlab.org/exp_prog/proposals/13/PR12-13-010.pdf).
- 652 [12] JLab experiment **E12-06-114**, Measurements of the Electron-Helicity Depen-
653 dent Cross Sections of Deeply Virtual Compton Scattering with CEBAF at 12
654 GeV, available online: [https://www.jlab.org/exp_prog/proposals/06/](https://www.jlab.org/exp_prog/proposals/06/PR12-06-114.pdf)
655 [PR12-06-114.pdf](https://www.jlab.org/exp_prog/proposals/06/PR12-06-114.pdf).

- 656 [13] JLab experiment **E12-13-007**, Measurement of SemiInclusive π^0 Production as
657 Validation of Factorization , available online: [https://www.jlab.org/exp_](https://www.jlab.org/exp_prog/proposals/13/PR12-13-007.pdf)
658 [prog/proposals/13/PR12-13-007.pdf](https://www.jlab.org/exp_prog/proposals/13/PR12-13-007.pdf).
- 659 [14] JLab experiment **E12-14-003**, Wide-angle Compton Scattering at 8 and 10
660 GeV Photon Energies, available online: [https://www.jlab.org/exp_prog/](https://www.jlab.org/exp_prog/proposals/14/PR12-14-003.pdf)
661 [proposals/14/PR12-14-003.pdf](https://www.jlab.org/exp_prog/proposals/14/PR12-14-003.pdf).
- 662 [15] JLab experiment **E12-17-008**, Polarization Observables in Wide-Angle Compton
663 Scattering at large s , t , and u , available online: [https://www.jlab.org/exp_](https://www.jlab.org/exp_prog/proposals/17/PR12-17-008.pdf)
664 [prog/proposals/17/PR12-17-008.pdf](https://www.jlab.org/exp_prog/proposals/17/PR12-17-008.pdf).
- 665 [16] JLab experiment **E12-14-005**, Wide Angle, Exclusive Photoproduction of π^0
666 Mesons, available online: [https://www.jlab.org/exp_prog/proposals/](https://www.jlab.org/exp_prog/proposals/14/PR12-14-005.pdf)
667 [14/PR12-14-005.pdf](https://www.jlab.org/exp_prog/proposals/14/PR12-14-005.pdf).
- 668 [17] M. Kubantsev, I. Larin, A. Gasparian, Performance of the PrimEx electromag-
669 netic calorimeter, AIP Conf. Proc. 867 (1) (2006) 51–58. arXiv:physics/
670 [0609201](https://arxiv.org/abs/0609201), doi:10.1063/1.2396938.
- 671 [18] A. Gasparian, A high performance hybrid electromagnetic calorimeter at Jef-
672 ferson Lab, in: 11th International Conference on Calorimetry in High-Energy
673 Physics (Calor 2004), 2004.
- 674 [19] Eljen Technology, Organic Scintillators, available online: [https:](https://eljentechnology.com)
675 [//eljentechnology.com](https://eljentechnology.com).
- 676 [20] V. Popov, H. Mkrtchyan, New photomultiplier active base for hall c jefferson
677 lab lead tungstate calorimeter, in: 2012 IEEE Nuclear Science Symposium and
678 Medical Imaging Conference Record (NSS/MIC), 2012, pp. 1177–1179. doi:
679 [10.1109/NSSMIC.2012.6551294](https://doi.org/10.1109/NSSMIC.2012.6551294).
- 680 [21] F. Barbosa, et al., A VME64x, 16-Channel, Pipelined 250 MSPS Flash ADC With
681 Switched Serial (VXS) Extension, Tech. rep., Jefferson Lab, Technical Report
682 GlueX-doc-1022 (hyperlink) (Apr. 2007).

- 683 [22] R. Brun, F. Rademakers, ROOT: An object oriented data analysis framework,
684 Nucl. Instrum. Meth. A 389 (1997) 81–86. doi:10.1016/S0168-9002(97)
685 00048-X.
- 686 [23] F. Barbosa, C. Hutton, A. Sitnikov, A. Somov, S. Somov, I. Tolstukhin, Pair spec-
687 trometer hodoscope for Hall D at Jefferson Lab, Nucl. Instrum. Meth. A 795
688 (2015) 376–380. doi:10.1016/j.nima.2015.06.012.
- 689 [24] A. Somov, Development of level-1 triggers for experiments at Jefferson Lab, AIP
690 Conf. Proc. 1560 (1) (2013) 700–702. doi:10.1063/1.4826876.
- 691 [25] J. Allison, et al., Recent developments in geant4, Nuclear Instruments and
692 Methods in Physics Research Section A: Accelerators, Spectrometers, Detectors
693 and Associated Equipment 835 (2016) 186–225. doi:https://doi.org/10.
694 1016/j.nima.2016.06.125.
- 695 [26] F. Barbosa, et al., Characterization of the NPS and CCAL readout , Tech.
696 rep., Jefferson Lab, GlueX-doc-3272, (2017), [https://halldweb.jlab.org/
697 doc-public/DocDB/ShowDocument?docid=3272](https://halldweb.jlab.org/doc-public/DocDB/ShowDocument?docid=3272).
- 698 [27] R. T. Jones, et al., A bootstrap method for gain calibration and resolution determi-
699 nation of a lead-glass calorimeter, Nucl. Instrum. Meth. A 566 (2006) 366–374.
700 doi:10.1016/j.nima.2006.07.061.
- 701 [28] A. Lednev, Separation of the overlapping electromagnetic showers in the cellular
702 gams-type calorimeters., Tech. rep., IHEP Protvino, Preprint IHEP (1993) 93-
703 153.
- 704 [29] F. Binon, et al., Hodoscope multi-photon spectrometer GAMS-2000, Nucl. In-
705 strument. Meth. A 248 (1986) 86. doi:10.1016/0168-9002(86)90501-2.
- 706 [30] A. Brunner, et al., A Cockcroft-Walton base for the FEU84-3 photomulti-
707 plier tube, Nucl. Instrum. Meth. A 414 (1998) 466–476. doi:10.1016/
708 S0168-9002(98)00651-2.

- 709 [31] O. Glamazdin, TOSCA simulation of the magnetic shielding of the FCAL insert ,
710 Tech. rep., Jefferson Lab, GlueX-doc-3561, (2018), [https://halldweb.jlab.
711 org/doc-private/DocDB/ShowDocument?docid=3561](https://halldweb.jlab.org/doc-private/DocDB/ShowDocument?docid=3561).
- 712 [32] W. Koska, S. W. Delchamps, J. Freeman, W. Kinney, D. Lewis, P. Limon, J. Strait,
713 I. Fiori, M. Gallinaro, Q. Shen, Evaluation of candidate photomultiplier tubes for
714 the upgrade of the CDF end plug calorimeter, Nucl. Instrum. Meth. A 406 (1998)
715 103–116. doi:10.1016/S0168-9002(97)01193-5.
- 716 [33] T. Horn, et al., Scintillating crystals for the Neutral Particle Spectrometer in Hall
717 C at JLab, Nucl. Instrum. Meth. A 956 (2020) 163375. arXiv:1911.11577,
718 doi:10.1016/j.nima.2019.163375.

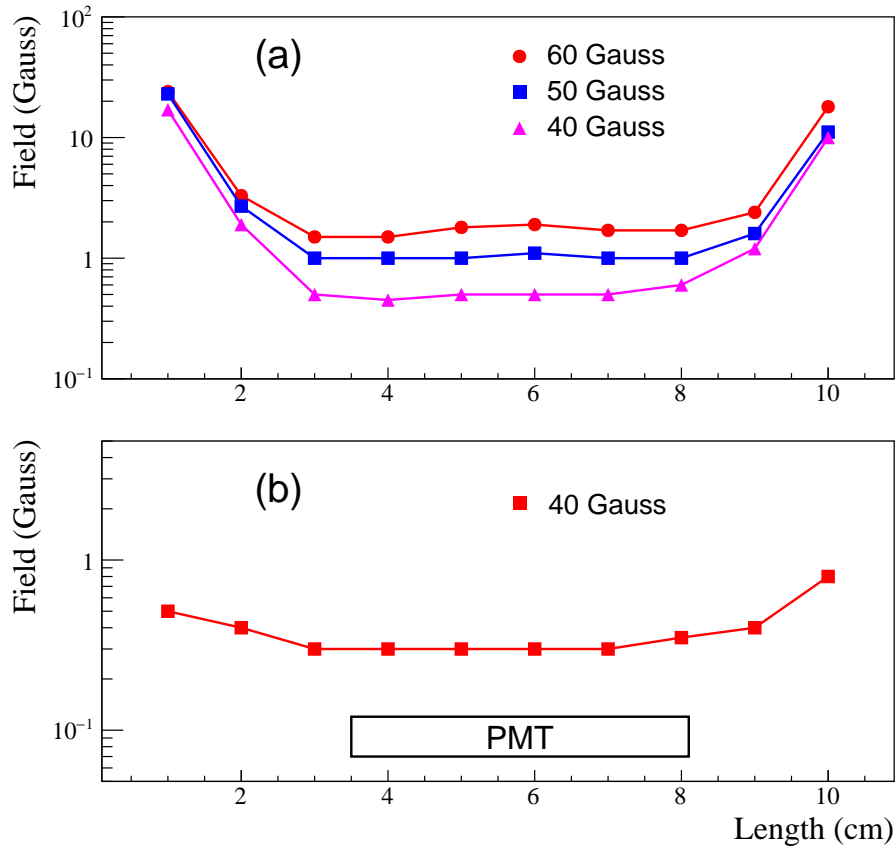


Figure 16: Magnetic field distribution inside the PMT shield housing as a function of the distance from the housing face. Plot (a) corresponds to the longitudinal field and plot (b) corresponds to the transverse field produced by the Helmholtz coils. Markers denote different values of the magnetic field generated by the Helmholtz coils.

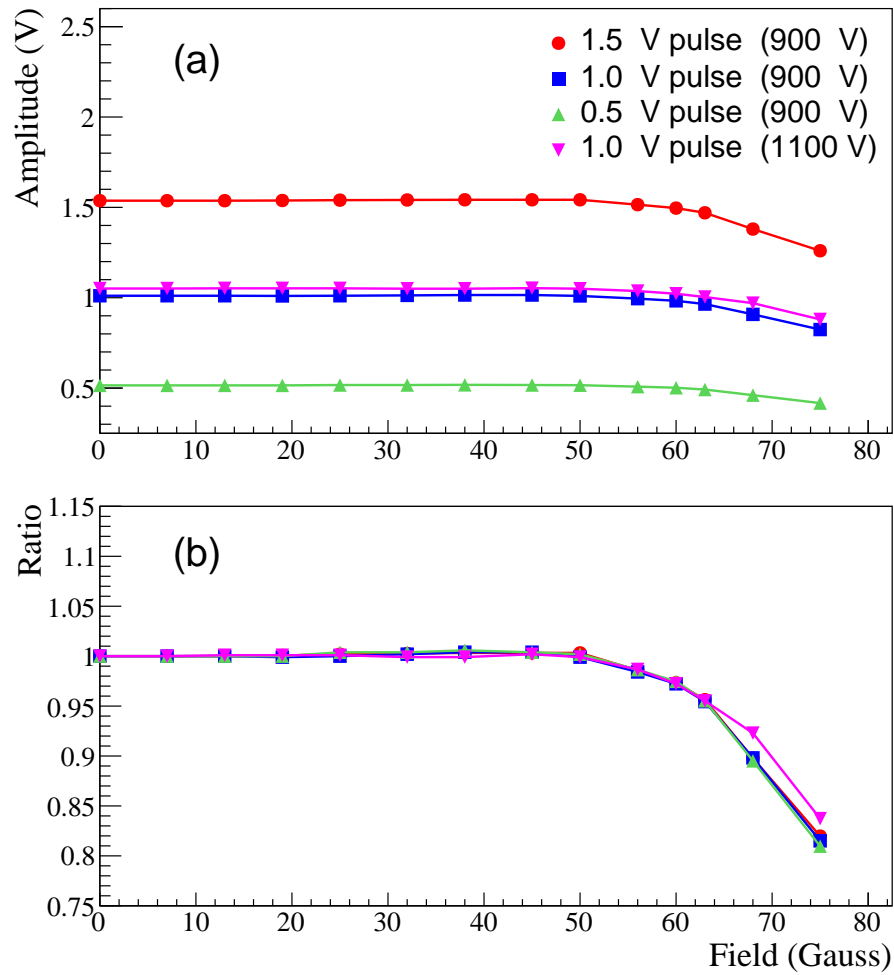


Figure 17: Signal amplitudes of shielded PMT induced by an LED as a function of the magnetic field (a). Amplitudes, normalized to measurements without magnetic field (b). The PMT response was measured for different intensities of light pulse and HV settings as shown by different polymarkers.

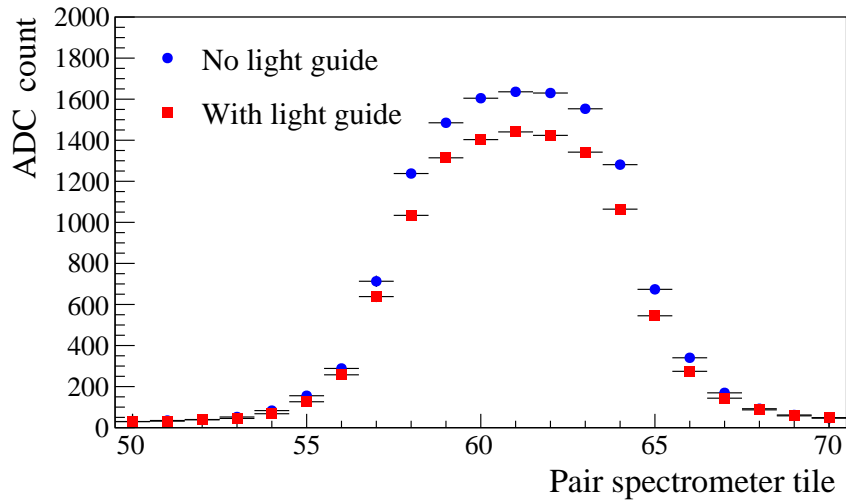


Figure 18: ADC amplitudes of the calorimeter module as a function of the pair spectrometer tile for two configurations: the PMT directly coupled to the PbWO₄ crystal (circles), and the PMT coupled to the module using optical light guide (boxes).

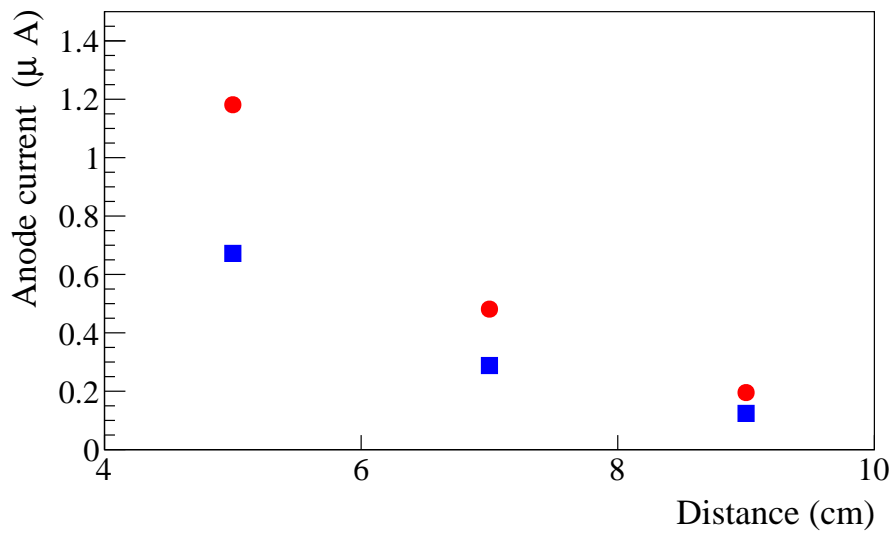


Figure 19: Typical PMT anode current of CCAL modules positioned at different distances from the beamline. Circles correspond to the nominal GlueX luminosity, boxes correspond to 60% of the nominal luminosity.